Physical insights into flicker noise in p-GaN gate AlGaN/GaN HEMTs: A temperature-dependent correlated carrier-number and mobility fluctuation model

Yi-Hui Song(宋怡慧)[1], Zhi-Gang Wang(汪志刚)[1,†], Yi-Jun Shi(施宜军)[2,‡], Yu-Chen Zhong(钟宇辰)[1], and Bo-Yu Zhan(詹柏瑜)[2]

[1] *School of Integrated Circuits Science and Engineering, Southwest Jiaotong University, Chengdu* 611756, *China*
[2] *China Electronic Product Reliability and Environmental Testing Research Institute, Guangzhou* 510610, *China*

(Received 9 July 2026; revised manuscript received 28 August 2026; accepted manuscript online 18 September 2026)

A temperature-dependent flicker $(1/f)$ noise model is developed for p-GaN gate AlGaN/GaN HEMTs by coupling trap-related fluctuation mechanisms: carrier-number fluctuation (CNF) and carrier-mobility fluctuation (CMF). Based on this, a dimensionless fluctuation-weighting factor is introduced to quantify the relative contribution of CNF and CMF as the two-dimensional electron gas (2DEG) density increases. The model naturally leads to three analytical regimes, corresponding to the low-, moderate-, and strong-2DEG regions. Experimental measurements performed over gate biases of 0.5–4.2 V, temperatures of 300–420 K, and frequencies of 1 Hz–10 kHz show good agreement with the proposed model. The proposed model provides a unified interpretation of bias-, temperature-, and frequency-dependent $1/f$ noise in p-GaN gate AlGaN/GaN HEMTs and offers a physical basis for trap-related mechanism characterization in normally-off GaN power devices.

Keywords: flicker $(1/f)$ noise, gallium nitride (GaN), high electron mobility transistor (HEMT), temperature, trap

PACS: 73.50.Td, 73.40.Kp, 72.20.Ee, 72.30.+q, 72.20.Ht

DOI: 10.1088/1674-1056/aea96b **CSTR:** 32038.14.CPB.aea96b

1. Introduction

AlGaN/GaN high-electron-mobility transistors (HEMTs) are promising candidates for high-frequency and high-temperature power conversion owing to the wide bandgap, high critical electric field, and high electron saturation velocity of GaN.[1–3] Moreover, the high-density two-dimensional electron gas (2DEG) formed at the AlGaN/GaN heterointerface enables low on-state resistance.[4] For practical power-electronic applications, normally-off operation is also highly desirable because it facilitates fail-safe operation and simplifies gate-drive design.[5] To meet this requirement, the p-GaN layer depletes the underlying 2DEG channel at zero gate bias (gate-to-source voltage, V_{GS}), thereby realizing enhancement-mode operation while retaining the transport advantages of the AlGaN/GaN heterostructure.[6] Consequently, p-GaN gate AlGaN/GaN HEMTs have attracted considerable interest for electric vehicles, data-center power supplies, renewable-energy converters, and compact high-frequency power-conversion systems.[7,8] Meanwhile, as these devices are operated at increasingly high voltages, switching frequencies, and junction temperatures, trap-related effects can induce threshold voltage (V_{TH}) instability, dynamic on-resistance degradation, and long-term reliability concerns.[9] In this context, flicker $(1/f)$ noise is particularly sensitive to such trap-carrier interactions and has therefore been widely employed as a nondestructive electrical probe of trap generation, trapping dynamics, and material/device quality in GaN HEMTs.[8,10–12] For example, stress-induced changes in $1/f$ noise, combined with electroluminescence characterization, have been employed to identify progressive trap generation in OFF-state-stressed AlGaN/GaN HEMTs, and noise-extracted trap parameters have shown consistency with independent material characterization techniques.[10,13] Beyond trap identification, $1/f$ noise measurements have also been used to extract transport-related parameters such as parasitic series resistance, indicating that noise characteristics contain information on carrier transport paths and device electrostatics.[14] Moreover, the correlation between $1/f$ noise and conventional electrical parameters, such as V_{TH} instability and dynamic on-resistance degradation, has been investigated to clarify how trap dynamics affect device stability.[15–19] Together, these findings establish $1/f$ noise as a powerful diagnostic tool for probing the microscopic fluctuation processes that are closely linked to device stability and reliability.

Despite decades of investigation into the $1/f$ noise, its exact physical origins are still unclear in most systems, and the debate over the origin of $1/f$ noise remains unresolved.

†Corresponding author. E-mail: zhigangwang@swjtu.edu.cn
‡Corresponding author. E-mail: syj20094870@sina.com

© 2026 Chinese Physical Society and IOP Publishing Ltd. All rights, including for text and data mining, AI training, and similar technologies, are reserved.

CPB Online In-Press

The Hooge model associates $1/f$ noise with carrier-mobility fluctuations (CMF),[12] whereas the McWhorter model relates it to carrier-number fluctuations (CNF) arising from trapping and detrapping.[20] Wong's review notes that different electronic devices can exhibit similar $1/f$ spectra despite distinct physical origins,[20] and that classical models such as those of Hooge and McWhorter are applicable only under specific conditions. This device dependence is also evident in GaN technologies: studies of AlGaN/GaN FinFETs and planar HEMTs show that the temperature dependence and dominant defect contributions to $1/f$ noise vary with device geometry and interface configuration.[21,22] Therefore, the quantitative applicability of a physical noise model established for one GaN HEMT architecture to another should be carefully evaluated by considering the device-specific electrostatics, charge-control relationship, carrier transport, and trap-carrier interactions. For p-GaN gate AlGaN/GaN HEMTs, $1/f$ noise is generally attributed to a combination of CNF and CMF. CNF originates from the random capture and emission of 2DEG carriers by traps, whereas CMF arises from fluctuations in carrier-scattering strength.[23] These two mechanisms are not necessarily independent, because a change in trap occupancy can simultaneously perturb the local carrier density and modify the carrier mobility through Coulomb scattering.[24] Their relative contributions therefore evolve continuously with gate bias V_{GS}. At low 2DEG density, the electrostatic modulation of the channel charge becomes dominant, and the normalized drain-current noise (S_{id}/I_{DS}^2) exhibits a dependence related to $(g_m/I_{DS})^2$.[10] Here, S_{id} denotes the noise power spectral density (PSD) of the drain-current fluctuation δI_{DS}, with units of A^2/Hz, while I_{DS} is the corresponding DC drain current and g_m is the transconductance. Accordingly, S_{id}/I_{DS}^2, with units of Hz^{-1}, represents the mean-square drain-current fluctuation per unit bandwidth normalized to the square of the DC current.[10,20] As the 2DEG density increases, the relative influence of CMF becomes more significant, leading to deviations from the conventional CNF scaling.[12] Most existing analytical models treat CNF and CMF as separate fluctuation sources and therefore cannot fully describe this bias- and temperature-dependent redistribution of the two contributions.[10,12,25,26] A unified framework that accounts for their correlated origin is consequently required to describe the transition between different fluctuation regimes in p-GaN gate HEMTs, thereby linking the experimentally observed noise evolution to specific trap-induced fluctuation mechanisms and providing physical guidance for low-noise operation optimization in normally-off GaN power devices.

In this work, a temperature-dependent $1/f$ noise model is developed for p-GaN gate AlGaN/GaN HEMTs by coupling trap-induced CNF and CMF. A dimensionless fluctuation-weighting factor is introduced to describe the relative weighting between the two fluctuation channels. Based on this factor, three operating regimes are derived, corresponding to CNF-dominated, coupled CNF–CMF, and CMF-dominated behavior. Measurements performed from 300 K to 420 K are used to evaluate the proposed model and identify the transition between different fluctuation regimes.

2. Flicker noise modeling

The measured $1/f$ noise is commonly described using the generalized relation[27]

$$\frac{S_{id}}{I_{DS}^2} = \frac{\alpha_H}{N f^{\gamma}}, \tag{1}$$

where α_H is the Hooge parameter, N is the total number of channel carriers, f is the frequency, and γ is the spectral exponent. Equation (1) describes the dependence of S_{id}/I_{DS}^2 on the carrier population and frequency.

In p-GaN gate AlGaN/GaN HEMTs, δI_{DS} originates from the random occupation fluctuation of charged traps (δN_T).[20] This single microscopic perturbation affects the channel through two correlated response channels. First, the trapped charge electrostatically perturbs the local 2DEG density, producing CNF. Second, the same charged trap modifies Coulomb scattering and thus perturbs the carrier mobility, producing CMF. Therefore, CNF and CMF should not be treated as two independent noise sources. Instead, they are two correlated responses driven by the same stochastic trap-occupation event.[28,29] Under this framework, δI_{DS} can be rewritten as a single-variable mapping:

$$\begin{aligned}\frac{\delta I_{DS}}{I_{DS}} &= \frac{\delta \mu_n(x)}{\mu_n(x)} + \frac{\delta n_c(x)}{n_c(x)} \\ &= \left(\frac{R}{n_c(x)} + \alpha \mu_n(x)\right) \delta N_T,\end{aligned} \tag{2}$$

where $n_c(x)$ is the local 2DEG density, $\mu_n(x)$ is the electron mobility, x is the channel position measured from the source side, R is the electrostatic coupling coefficient between the fluctuating trapped charge and the 2DEG, and α is the mobility-scattering coefficient associated with trap-induced Coulomb scattering. Therefore, in Eq. (2), R/n_c represents the CNF-related fluctuation amplitude, whereas $\alpha\mu_n$ represents the CMF-related fluctuation amplitude. Their relative importance is therefore controlled by the carrier-density-dependent ratio $\alpha\mu_n n_c/R$. This ratio provides the physical basis for the following regional analysis. When n_c is small, R/n_c is large, and CNF dominates. As n_c increases, the electrostatic perturbation is screened, R/n_c decreases, and the CMF contribution becomes increasingly important.

According to the distributed trap-relaxation derivation in Appendix B, the corresponding local current-fluctuation spec-

CPB Online In-Press

trum is

$$S_{\delta \mathrm{id}}(x,f) = \frac{S_{\delta \mathrm{NT}}(f)}{WL^2}\left(\frac{\delta I_{\mathrm{DS}}}{\delta N_{\mathrm{T}}}\right)^2 = \frac{kTI_{\mathrm{DS}}^2 N_{\mathrm{T}}(E_{\mathrm{F}},T)}{WL^2\lambda_{\mathrm{t}} f^{\gamma}}\left(\frac{R}{n_{\mathrm{c}}(x)}+\alpha\mu_{\mathrm{n}}(x)\right)^2, \quad (3)$$

where $S_{\delta \mathrm{NT}}$ is the trap-occupation noise spectrum as expressed in (B4), k is Boltzmann's constant, T is the temperature in Kelvin, $N_{\mathrm{T}}(E_{\mathrm{F}}, T)$ is the effective trap density within the thermal energy window around the local Fermi level E_{F}, λ_{t} is the tunneling parameter, W is the device width, and L is the channel length. To distinguish the relative contributions of CNF and CMF, a dimensionless fluctuation-weighting factor is defined as

$$\Gamma(x,T) = \left(1+\frac{\alpha\mu_{\mathrm{n}}(x)n_{\mathrm{c}}(x)}{R}\right)^2 = 1+2\frac{\alpha\mu_{\mathrm{n}}(x)n_{\mathrm{c}}(x)}{R}+\left(\frac{\alpha\mu_{\mathrm{n}}(x)n_{\mathrm{c}}(x)}{R}\right)^2. \quad (4)$$

Using current continuity $\mathrm{d}x = (qn_{\mathrm{c}}\mu_{\mathrm{n}}W/I_{\mathrm{DS}})\mathrm{d}V_{\mathrm{c}}$, where q is the elementary charge, and V_{c} is the local channel potential, the total S_{id} can be obtained by integrating the local contribution along the channel:

$$S_{\mathrm{id}}(f) = \frac{kTI_{\mathrm{DS}}^2}{\lambda_{\mathrm{t}}WL^2 f^{\gamma}}\int_0^L N_{\mathrm{T}}(E_{\mathrm{F}},T)\left(\frac{R}{n_{\mathrm{c}}(x)}+\alpha\mu_{\mathrm{n}}(x)\right)^2\mathrm{d}x = \frac{kTqI_{\mathrm{DS}}}{\lambda_{\mathrm{t}}L^2 f^{\gamma}}\int_0^{V_{\mathrm{DS,eff}}}\frac{\mu_{\mathrm{n}}R^2}{n_{\mathrm{c}}}N_{\mathrm{T}}(E_{\mathrm{F}},T)\Gamma(x,T)\mathrm{d}V_{\mathrm{c}}, \quad (5)$$

where $V_{\mathrm{DS,eff}}$ is the effective potential drop across the gated channel. According to Eq. (5), the $1/f$ noise is jointly governed by trap occupation,[11] 2DEG charge control,[20] carrier mobility,[25] and the relative weighting between CNF and CMF.[28] In addition, temperature can simultaneously modify several quantities in Eq. (5), including the trap occupation distribution, the channel carrier mobility, the 2DEG density, and the relaxation-time distribution determining γ. Therefore, temperature affects not only the overall noise amplitude, but also the apparent transition between different fluctuation regimes. To obtain explicit analytical expressions, the differential relationship between the local channel charge and channel potential is written as

$$q\mathrm{d}n_{\mathrm{c}} = -C_{2\mathrm{D}}\mathrm{d}V_{\mathrm{c}}, \quad (6)$$

where $C_{2\mathrm{D}}$ is the effective channel-averaged differential gate-to-2DEG capacitance. Substituting Eq. (6) into Eq. (5), the resulting S_{id} is

$$S_{\mathrm{id}}(f) = S_0\int_{n_{\mathrm{D}}}^{n_{\mathrm{S}}}\frac{\mu_{\mathrm{n}}R^2}{n_{\mathrm{c}}}\Gamma(x,T)\mathrm{d}n_{\mathrm{c}}, \quad (7)$$

where $S_0 = kTI_{\mathrm{DS}}q^2N_{\mathrm{T}}(E_{\mathrm{F}},T)/(\lambda_{\mathrm{t}}C_{2\mathrm{D}}L^2f^{\gamma})$, $n_{\mathrm{S}} = n_{\mathrm{c}}(x=0)$, and $n_{\mathrm{D}} = n_{\mathrm{c}}(x=L)$ are the source- and drain-side carrier densities, respectively. Equation (7) represents a unified stochastic transport expression for the $1/f$ noise under arbitrary bias conditions. Based on the density of 2DEG, the subsequent regional expressions are derived by systematically expanding Eq. (7).

2.1. Low-2DEG region

In the low-2DEG region (near-threshold operating ranges), V_{GS} is relatively small and only a weak 2DEG channel is formed. The channel carrier density n_{c} remains extremely low. Therefore, a small trap-occupation fluctuation produces a large fractional perturbation in the local carrier density. Mathematically, this corresponds to $\alpha\mu_{\mathrm{n}}n_{\mathrm{c}}/R \ll 1$ (equivalently $R/n_{\mathrm{c}} \gg \alpha\mu_{\mathrm{n}}$). Then Eq. (4) becomes $\Gamma \approx 1$ and Eq. (7) reduces to

$$S_{\mathrm{id}}(f) = S_0\mu_{\mathrm{n}}R^2\ln\left(\frac{n_{\mathrm{S}}}{n_{\mathrm{D}}}\right). \quad (8)$$

Equation (8) indicates that the $1/f$ noise in the low-2DEG region is primarily controlled by the inverse dependence of the CNF amplitude on the local 2DEG density. Since the drain-side carrier density n_{D} is generally lower than the source-side density n_{S}, the drain-side channel is more sensitive to trap-induced electrostatic modulation. As the effective gate voltage $V_{\mathrm{GT}} = V_{\mathrm{GS}} - V_{\mathrm{TH}}$ increases, both n_{S} and n_{D} increase, which reduces the relative CNF. Nevertheless, R/n_{c} remains larger than the CMF-related term $\alpha\mu_{\mathrm{n}}$ throughout this region. Consequently, the $1/f$ noise decreases with increasing V_{GT}, and the dominant noise mechanism remains CNF.

The corresponding α_{H} in this region can be expressed as

$$\alpha_{\mathrm{H}} = \alpha_{\mathrm{H0}}\mu_{\mathrm{n}}R^2\ln\left(\frac{n_{\mathrm{S}}}{n_{\mathrm{D}}}\right), \quad (9)$$

where $\alpha_{\mathrm{H0}} = kTq^2N_{\mathrm{T}}(E_{\mathrm{F}},T)/(\lambda_{\mathrm{t}}C_{2\mathrm{D}}I_{\mathrm{DS}}^2L^2)$. This expression shows that α_{H} should decrease as the 2DEG density increases, because the same trap-occupation event produces a smaller fractional carrier-number perturbation in a denser channel.

2.2. Moderate-2DEG region

In the moderate-2DEG region, increasing V_{GT} produces a substantial rise in the 2DEG density. Consequently, the CNF amplitude R/n_{c} decreases, whereas the relative influence of the CMF amplitude $\alpha\mu_{\mathrm{n}}$ becomes more pronounced. The two local fluctuation amplitudes become comparable when $\alpha\mu_{\mathrm{n}} \approx R/n_{\mathrm{c}}$. In this regime, neither CNF nor CMF can be neglected. Therefore, the CNF self term, the correlated CNF–CMF cross term, and the CMF self term must all be retained:

$$S_{\mathrm{id}}(f) = S_0\int_{n_{\mathrm{D}}}^{n_{\mathrm{S}}}\left(\frac{\mu_{\mathrm{n}}R^2}{n_{\mathrm{c}}}+2\alpha\mu_{\mathrm{n}}^2R+n_{\mathrm{c}}\alpha^2\mu_{\mathrm{n}}^3\right)\mathrm{d}n_{\mathrm{c}} = S_0\left[\mu_{\mathrm{n}}R^2\ln\left(\frac{n_{\mathrm{S}}}{n_{\mathrm{D}}}\right)+2\alpha\mu_{\mathrm{n}}^2R(n_{\mathrm{S}}-n_{\mathrm{D}})+\frac{\alpha^2\mu_{\mathrm{n}}^3}{2}\left(n_{\mathrm{S}}^2-n_{\mathrm{D}}^2\right)\right]. \quad (10)$$

CPB Online In-Press

The three terms in Eq. (10) are the channel-integrated components of a single correlated fluctuation process. Near the lower boundary of the moderate-2DEG region ($R/n_c > \alpha\mu_n$), the CNF-associated term provides the principal contribution. As V_{GT} increases, the cross term and the CMF-associated term gain increasing relative importance. The condition $R/n_c \approx \alpha\mu_n$ indicates that the two local fluctuation amplitudes are of the same order and defines the local CNF–CMF crossover.

The corresponding α_H is

$$\alpha_H = \alpha_{H0}\left[\mu_n R^2 \ln\left(\frac{n_S}{n_D}\right) + 2\alpha\mu_n^2 R\left(n_S - n_D\right) + \frac{\alpha^2\mu_n^3}{2}\left(n_S^2 - n_D^2\right)\right]. \tag{11}$$

Equation (11) provides a direct way to compare the model with the measured α_H. In particular, the minimum of α_H is expected to appear near the bias point where the CNF-related amplitude and the CMF-related amplitude become comparable ($\alpha\mu_n n_c/R \approx 1$).

2.3. Strong-2DEG region

At sufficiently high V_{GT}, the 2DEG density becomes large and the electrostatic perturbation induced by trap occupation is effectively screened. In this case, $\alpha\mu_n n_c/R \gg 1$ (equivalently $R/n_c \ll \alpha\mu_n$) and the dimensionless fluctuation-weighting factor reduces to $\Gamma \approx (\alpha\mu_n n_c/R)^2$. Under this asymptotic condition, the CNF-associated and cross terms in Eq. (10) become small relative to the CMF-associated term. Therefore, S_{id} in the strong-2DEG region can be expressed as

$$S_{id}(f) = S_0 \frac{\alpha^2\mu_n^3\left(n_S^2 - n_D^2\right)}{2}. \tag{12}$$

In this region, further increase in V_{GT} only weakly modifies the channel charge because the differential charge response decreases at high 2DEG density. Meanwhile, mobility degradation associated with enhanced Coulomb scattering becomes increasingly relevant. The weak increase of the charge-dependent factor and the reduction of μ_n partially compensate each other, leading to a much weaker V_{GT} dependence of the measured noise.

The corresponding α_H is

$$\alpha_H = \alpha_{H0} \frac{\alpha^2\mu_n^3\left(n_S^2 - n_D^2\right)}{2}. \tag{13}$$

Equations (8)–(13) will be evaluated in Section 3 through direct comparisons between the calculated and measured noise characteristics over different frequencies, gate biases, and temperatures, together with the extracted α_H. These complementary comparisons examine both the predictive capability of the model for the experimentally observed noise evolution and its physical description of the CNF–CMF transition. Therefore, the three-regime analysis not only describes the bias dependence of $1/f$ noise but also provides a practical method for identifying the dominant fluctuation mechanism and locating the CNF–CMF transition boundary.

3. Experimental results and discussion

The device under test (DUT) is the investigated p-GaN gate AlGaN/GaN HEMT. A simplified schematic of the device structure is shown in Fig. 1(a), together with the corresponding scanning electron microscopy (SEM) images in Fig. 1(c). Figure 1(b) shows the measured transfer characteristics at 300 K, together with the extracted V_{TH} from 300 K to 420 K in the inset, providing the basic electrical characteristics for determining the gate-bias conditions used in the subsequent noise analysis. The experimental setup for the $1/f$ noise characterization is shown in Fig. 1(d). The DUT is mounted in a Keysight 16442B test fixture and connected to a Primarius FS-Pro semiconductor parameter analyzer, which integrates high-precision DC I–V characterization, high-speed time-domain signal acquisition, and $1/f$ noise measurement capabilities in the same system. The gate and drain terminals are biased by the source-measurement units of the analyzer to establish the required V_{GS} and V_{DS}, while the corresponding I_{DS} is simultaneously monitored. After the electrical response and device temperature reach steady state at each operating condition, δI_{DS} is acquired and analyzed using the integrated $1/f$ noise measurement function, from which S_{id} is obtained as a function of frequency.[30] The noise measurements are performed over a frequency range of 1 Hz–100 kHz and a temperature range of 300–420 K after electrical and thermal steady state is reached at each bias and temperature condition.

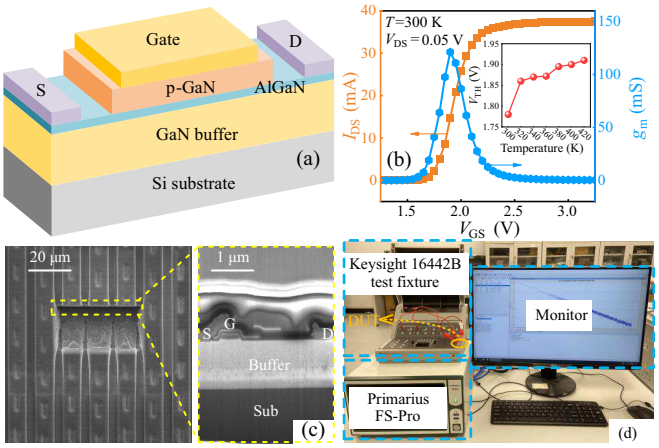


Fig. 1. (a) Simplified schematic of the investigated p-GaN gate AlGaN/GaN HEMT structure. (b) Measured I_{DS}–V_{GS} and g_m–V_{GS} characteristics. Inset: extracted V_{TH} as a function of temperature. (c) SEM images of the tested p-GaN gate HEMT. (d) Experimental setup for $1/f$ noise measurements using the Primarius FS-Pro semiconductor parameter analyzer and Keysight 16442B test fixture. The system provides a noise measurement bandwidth up to 100 kHz in the high-precision mode, with a minimum noise PSD resolution of 2×10^{-28} A^2/Hz and a frequency resolution of 1 mHz.[30]

CPB Online In-Press

The experimental discussion is organized as follows. First, the coexistence of CNF and CMF is examined by comparing S_{id} under different drain biases. Second, the frequency- and gate-bias-dependent normalized noise characteristics are used to show how the overall fluctuation amplitude evolves as the channel is gradually turned on. Third, the V_{GT}-dependent scaling of S_{id}/I_{DS}^2 is used to identify the three regimes predicted in Section 2. Finally, the extracted Hooge parameter is compared with the analytical expressions (9), (11), and (13), providing a quantitative indicator of the CNF–CMF transition boundary.

4. Bias-dependent noise characteristics

Figure 2 compares S_{id} under different V_{DS} biases in the low- and moderate-2DEG regions. In the low-2DEG region ($V_{GS} = 1.4$ V $< V_{TH}$), S_{id} decreases monotonically with increasing V_{DS} as shown in Fig. 2(a). In contrast, as shown in Fig. 2(b), when the device operates in the moderate-2DEG region ($V_{GS} = 2.6$ V), the dependence of S_{id} on V_{DS} becomes non-monotonic. A distinct maximum appears as the channel potential and local 2DEG density are redistributed along the channel. This non-monotonic behavior cannot be fully explained by the low-density CNF asymptote alone. According to Eq. (10), it arises because the CNF term, the correlated CNF–CMF cross term, and the CMF term contribute simultaneously in the moderate-2DEG region. Therefore, Fig. 2 indicates that CNF and CMF coexist and that their relative weights evolve with bias.

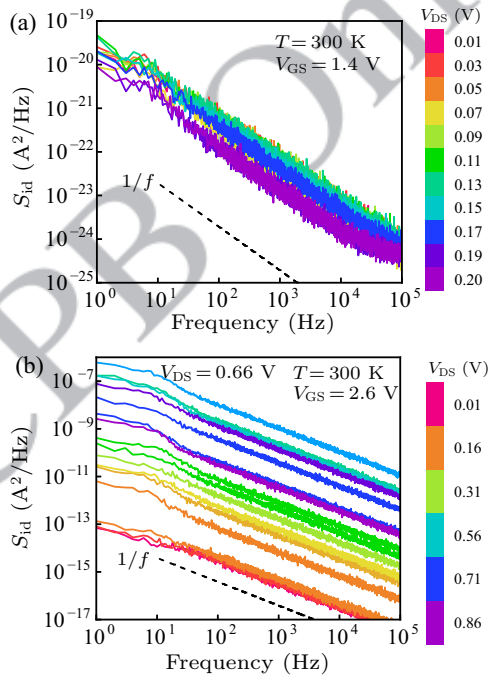


Fig. 2. Drain-current noise power spectral density (S_{id}) measured at room temperature (300 K). (a) Low-2DEG region ($V_{GS} = 1.4$ V) for V_{DS} ranging from 0.01 V to 0.20 V in steps of 0.01 V. In this region, S_{id} decreases monotonically with increasing V_{DS}. (b) Moderate-2DEG region ($V_{GS} = 2.6$ V) for V_{DS} ranging from 0.01 V to 0.86 V in steps of 0.05 V. In this region, S_{id} does not exhibit a monotonic dependence on V_{DS}. The minimum S_{id} is observed at $V_{DS} = 0.01$ V and the maximum at $V_{DS} = 0.66$ V.

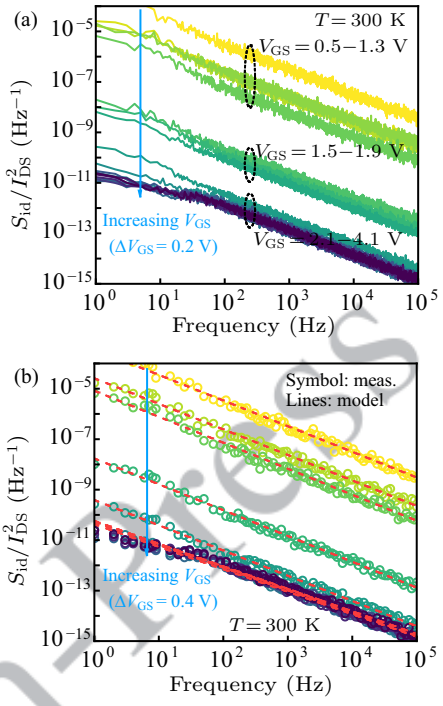


Fig. 3. (a) Normalized drain-current noise power spectral density (S_{id}/I_{DS}^2) as a function of frequency for V_{GS} ranging from 0.5 V to 4.1 V in steps of 0.2 V at 300 K. As V_{GS} increases, the magnitude of S_{id}/I_{DS}^2 decreases monotonically and eventually stabilizes. (b) Comparison of measured (symbols) and calculated (dashed lines) S_{id}/I_{DS}^2 for V_{GS} ranging from 0.5 V to 4.1 V in steps of 0.4 V. The experimental data in (b) are taken from (a).

To examine how the noise evolves with gate bias, Fig. 3(a) presents the normalized noise S_{id}/I_{DS}^2 as a function of frequency for V_{GS} ranging from 0.5 V to 4.1 V at 300 K, and Fig. 3(b) compares the measured and calculated S_{id}/I_{DS}^2 at different V_{GS}. Good agreement is obtained over the measured frequency and gate-bias ranges. In particular, the calculated spectra reproduce both the frequency dependence of S_{id}/I_{DS}^2 at each gate bias and its systematic reduction with increasing V_{GS}, indicating that the proposed model captures the coupled frequency- and bias-dependent evolution of the normalized noise. The magnitude of S_{id}/I_{DS}^2 decreases monotonically with increasing V_{GS} and eventually stabilizes at high gate biases. This trend reflects the progressive reduction of the relative current fluctuation as the channel is turned on and the 2DEG density increases. More specifically, the measured curves can be divided into three gate-bias ranges. For $V_{GS} = 0.5$–1.3 V, the device remains in the off-state (V_{TH} is approximately 1.78 V at 300 K, as shown in Fig. 1(b)). In this range, the drain current I_{DS} is extremely small, leading to a large S_{id}/I_{DS}^2. When V_{GS} increases to 1.5–1.9 V, S_{id}/I_{DS}^2 decreases rapidly with increasing V_{GS}. As V_{GS} further increases to 2.1–4.1 V, the normalized noise becomes much lower and varies only weakly with further increase in V_{GS}, indicating that the relative fluctuation amplitude is gradually suppressed in the high-density channel. It is also noted that the spectra within each gate-bias range remain close to each other, and their frequency dependences are similar over the measured bias range. This indicates that in-

CPB Online In Press

creasing V_{GS} mainly changes the magnitude of the normalized noise without introducing an additional noise component. The simultaneous agreement in spectral shape and noise magnitude further supports the proposed model over both the frequency and gate-bias domains at 300 K and provides the basis for its subsequent temperature-dependent evaluation.

5. Temperature-dependent noise characteristics

To examine the temperature dependence of $1/f$ noise, Fig. 4 compares the measured and calculated S_{id} at $V_{GS} =$ 2.6 V over the temperature range from 300 K to 420 K. As shown in Fig. 4, the model reproduces the temperature-dependent evolution of S_{id} magnitude from 300 K to 420 K, supporting the temperature dependences incorporated through the effective trap occupation, mobility, and channel-charge terms in Eq. (5). Together with Fig. 3(b), these comparisons validate the model over gate-bias, frequency, and temperature domains.

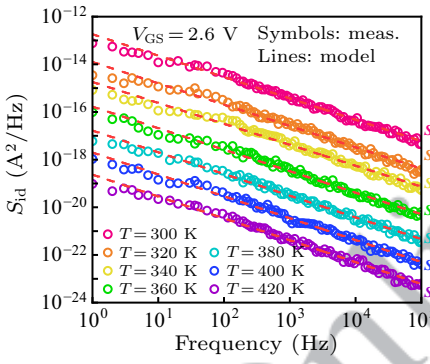


Fig. 4. Measured (symbols) and calculated (dashed lines) drain-current noise power spectral density (S_{id}) measured at $V_{GS} = 2.6$ V over a temperature range from 300 K to 420 K in steps of 20 K. Although S_{id} increases slightly with temperature, the total variation between 300 K and 420 K remains below one order of magnitude (successive spectra are vertically shifted by the indicated factors for clarity).

To further relate the gate-bias-dependent trend to the underlying fluctuation mechanism, Fig. 5 presents S_{id}/I_{DS}^2 as a function of I_{DS} at 25 Hz and 100 Hz over the temperature range from 300 K to 420 K. Within the CNF framework, trapping and detrapping events perturb the channel electrostatics and can be represented by an equivalent gate-voltage fluctuation.[12] Since the resulting δI_{DS} satisfies $\delta I_{DS} = g_m \delta V_{GS}$, the normalized noise follows $S_{id}/I_{DS}^2 \propto (g_m/I_{DS})^2 S_{VG}$,[8,28] where S_{VG} denotes the equivalent input-referred voltage-noise PSD. The $(g_m/I_{DS})^2$ dependence therefore provides a conventional reference for evaluating the CNF contribution: agreement with this scaling is consistent with CNF-controlled fluctuations, whereas a systematic departure suggests that additional fluctuation contributions become involved.[10,20] As shown in Fig. 5, two distinct behaviors can be identified. In the low-current region ($I_{DS} < 0.01$ A), the normalized noise approximately follows the $(g_m/I_{DS})^2$ trend (solid curves in Fig. 5), indicating a substantial CNF contribution at low channel density, consistent with the CNF-dominated limit of Eq. (8).[10] At higher current levels ($I_{DS} >$ 0.01 A), systematic deviations from the $(g_m/I_{DS})^2$ trend appear. Such a deviation indicates that CNF alone is no longer sufficient to describe the measured noise and is consistent with the transition predicted by the proposed model. According to Eq. (10), the noise in the moderate- and strong-2DEG regions contains not only the CNF term but also the correlated CNF–CMF cross term and the CMF term.[28] In addition, the normalized noise shows an overall decreasing trend with increasing temperature, indicating that the relative current fluctuation is gradually suppressed at elevated temperatures.

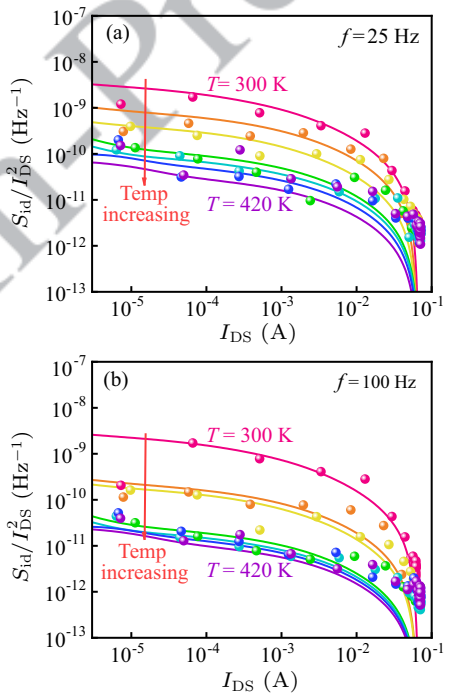


Fig. 5. Normalized drain-current noise power spectral density (S_{id}/I_{DS}^2) as a function of drain current (I_{DS}) over a temperature range from 300 K to 420 K in steps of 20 K at (a) 25 Hz and (b) 100 Hz. The noise power density decreases monotonically with increasing temperature. The solid curves indicate the corresponding $(g_m/I_{DS})^2$ trends. Deviations become more evident in the high-current region. At 25 Hz, S_{id}/I_{DS}^2 varies more uniformly with temperature than that at 100 Hz. At 100 Hz, in the temperature range from 380 K to 420 K, S_{id}/I_{DS}^2 remains almost unchanged with temperature.

Figure 6 further examines the temperature dependence of S_{id}/I_{DS}^2 at fixed gate biases from $V_{GS} = 1.5$ V to 4.2 V. At low V_{GS}, especially from 1.5 V to 1.9 V, the normalized noise decreases markedly as temperature increases from 300 K to 380 K. Above 380 K, the temperature dependence becomes weaker. As V_{GS} increases, both the magnitude and temperature sensitivity of S_{id}/I_{DS}^2 are reduced. At sufficiently high V_{GS}, the normalized noise becomes nearly temperature independent over the measured range, which is consistent with the stabilized S_{id}/I_{DS}^2 at high gate biases in Fig. 3. According to Eq. (4), this occurs because the high-density 2DEG screens the electrostatic perturbation associated with CNF, while the relative

CPB Online In Press

importance of CMF increases. Overall, Fig. 6 indicates that temperature has a stronger effect in the CNF-dominated weak-channel regime and a weaker effect in the CMF-influenced high-density regime.

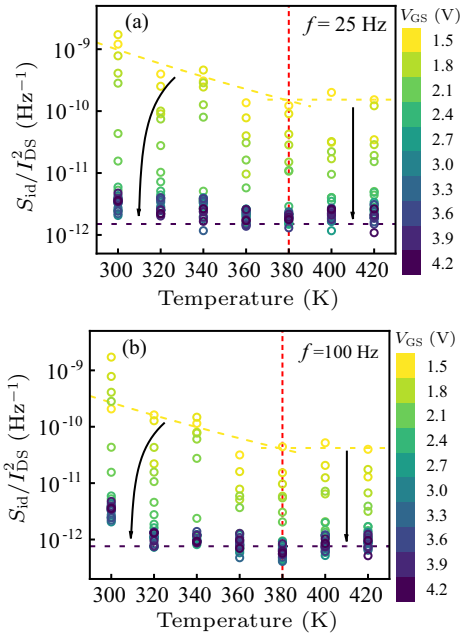


Fig. 6. Normalized drain-current noise power spectral density (S_{id}/I_{DS}^2) as a function of temperature for V_{GS} ranging from 1.5 V to 4.2 V at (a) 25 Hz and (b) 100 Hz. At lower V_{GS} (1.5 V to 1.9 V), S_{id}/I_{DS}^2 exhibits a pronounced decreasing trend with increasing temperature from 300 K to 380 K. Beyond 380 K, the normalized noise power becomes largely stable and shows little further temperature dependence. As V_{GS} increases, the magnitude of S_{id}/I_{DS}^2 decreases, and its decreasing trend over the 300–380 K range gradually weakens. For large V_{GS} (beyond 3.8 V), the normalized noise power almost remains constant across the entire measured temperature range.

6. Noise behavior in three regimes

Figure 7 presents S_{id}/I_{DS}^2 as a function of V_{GT}. Based on the different power-law dependence,[31,32] the measured curves can be divided into three regimes, consistent with the model derived in Section 2. In the low-2DEG region (0.01 V $\leq V_{GT} <$ 0.14 V), the normalized noise exhibits a weak power-law dependence, approximately $V_{GT}^{-0.5}$ at 300 K and $V_{GT}^{-0.2}$ at 420 K. The relatively weak slope indicates that, although CNF dominates in this region, the available 2DEG density is still limited and the effective channel is strongly influenced by near-threshold electrostatics. In the moderate-2DEG region (0.14 V $\leq V_{GT} <$ 0.67 V), the gate dependence becomes significantly stronger, with the exponent varying from approximately -3 at 300 K to -1 at 420 K. As shown in Eq. (10), the moderate-2DEG region contains three terms with different dependences on n_S, n_D, and μ_n: the CNF term, the correlated CNF–CMF cross term, and the CMF term. As V_{GT} increases, the relative weights of these terms change rapidly. This redistribution produces the steep apparent power-law dependence observed in Fig. 7. In the strong-2DEG regime ($V_{GT} \geq 0.67$ V), S_{id}/I_{DS}^2 becomes nearly independent of V_{GT}, indicating that further increases in channel charge density no longer significantly affect the fluctuation strength due to screening of electrostatic noise and the increasing dominance of CMF. Overall, these three regimes are consistent with the analysis in Section 2, where the evolution of noise behavior is governed by the carrier-density-dependent weighting between CNF- and CMF-related mechanisms.

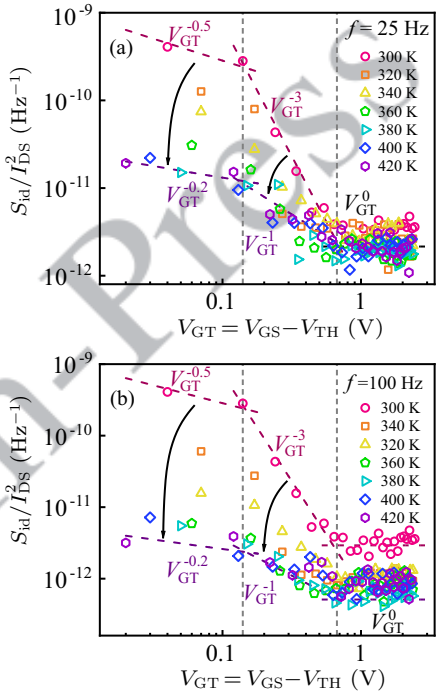


Fig. 7. Normalized drain-current noise power spectral density (S_{id}/I_{DS}^2) as a function of $V_{GT} = V_{GS} - V_{TH}$ over a temperature range from 300 K to 420 K in steps of 20 K at (a) 25 Hz and (b) 100 Hz. Across the entire measured V_{GT} range (0.01 V to 2.45 V), S_{id}/I_{DS}^2 decreases monotonically with increasing temperature. As V_{GT} increases, the normalized noise power progressively decreases and eventually stabilizes at higher V_{GT} values. The dependence on V_{GT} exhibits distinct regimes, with the corresponding power-law slopes varying systematically with temperature. In the low-2DEG region (0.01 V $\leq V_{GT} <$ 0.14 V), S_{id}/I_{DS}^2 follows approximately $V_{GT}^{-0.5}$ at 300 K; this dependence weakens with rising temperature, becoming $V_{GT}^{-0.2}$ at 420 K. In the moderate-2DEG region, the dependence becomes steeper, scaling as V_{GT}^{-3} at 300 K and as V_{GT}^{-1} at 420 K. In the strong-2DEG ($V_{GT} \geq 0.67$ V), S_{id}/I_{DS}^2 remains nearly independent of V_{GT} (except for S_{id}/I_{DS}^2 at 100 Hz and 300 K).

While Fig. 7 identifies the regime boundaries based on power-law scaling of S_{id}/I_{DS}^2, the extracted $\alpha_H = N \cdot f^{\gamma} \cdot S_{id}/I_{DS}^2$ in Fig. 8 provides a more quantitative indicator of the effective carrier-population-normalized noise strength. These boundaries are therefore determined independently of α_H, while the evolution of α_H provides additional physical support for the regime classification. As shown in Fig. 4, the noise follows a $1/f$ dependence at 10 kHz, which means the spectral exponent $\gamma = 1$ here. Across the entire measured V_{GT} range (0.01–2.45 V), α_H first decreases with V_{GT}, reaches a minimum near $V_{GT} \approx 0.67$ V, and then increases. In the low-to-moderate V_{GT} region (0.01–0.67 V), α_H decreases as V_{GT}^{-1} at 300 K, and the dependence weakens to $V_{GT}^{-0.7}$ at 420 K. Notably, the minimum of α_H approximately coincides with

CPB Online In-Press

the upper regime boundary independently identified from the power-law scaling in Fig. 7. According to Eq. (11), this minimum corresponds to the bias condition where the CNF amplitude R/n_c and the CMF amplitude $\alpha\mu_n$ become comparable. Therefore, the minimum of α_H provides an experimental marker for the CNF–CMF crossover. At higher V_{GT}, α_H increases approximately as V_{GT}^1, indicating that the CMF-related contribution becomes increasingly important in the strong-2DEG region. Although small temperature-dependent shifts in the transition positions are observed, the characteristic boundaries remain close to $V_{GT} \approx 0.67$ V. The good agreement between the measured data and model calculation confirms that the proposed CNF–CMF framework captures the bias-dependent noise behavior.

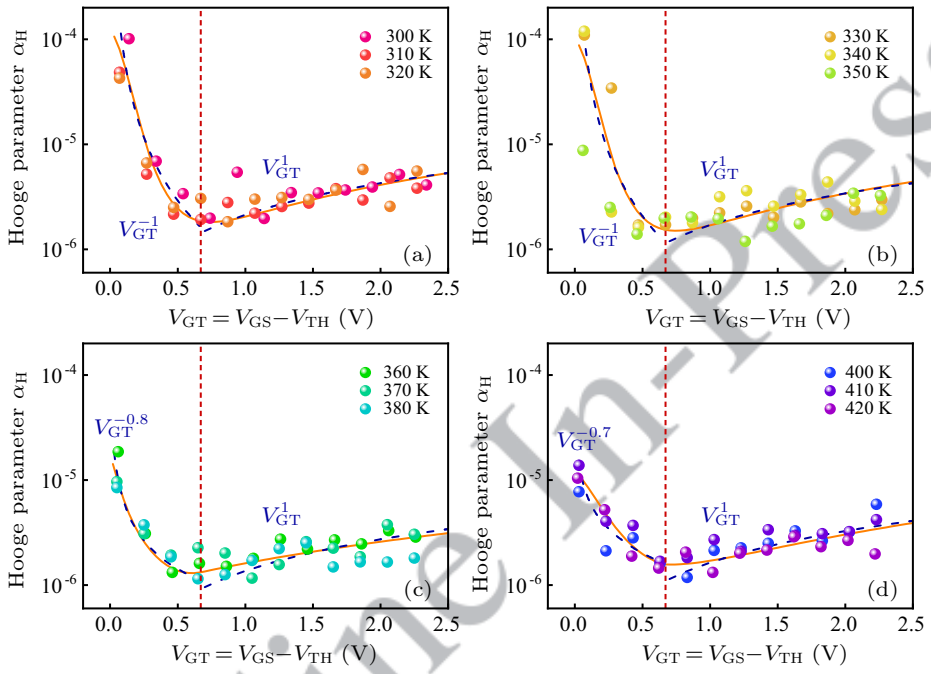


Fig. 8. Hooge parameter α_H as a function of $V_{GT} = V_{GS} - V_{TH}$ at (a) 300–320 K, (b) 330–350 K, (c) 360–380 K, and (d) 400–420 K. The symbols denote the experimentally values. The solid curves represent the results calculated from Eqs. (9), (11), and (13), whereas the dashed curves show the corresponding empirical fitting results. Across the entire measured V_{GT} range (0.01 V to 2.45 V), α_H first decreases and then increases. Overall, α_H decreases with rising temperature. In the low- and moderate-V_{GT} region (0.01 V–0.67 V), α_H follows approximately V_{GT}^{-1} at 300 K; this dependence weakens with rising temperature, becoming $V_{GT}^{-0.7}$ at 420 K. In the high-V_{GT} (beyond 0.67 V), α_H follows approximately V_{GT}^1 for all temperatures.

7. Conclusion

A temperature-dependent $1/f$ noise model is developed for p-GaN gate AlGaN/GaN HEMTs by treating trap-induced CNF and CMF as two correlated response channels driven by the same trap-occupation fluctuation. A dimensionless fluctuation-weighting factor is introduced to quantify the relative weighting between CNF and CMF, thereby describing the continuous transition from CNF-dominated behavior to CMF-dominated behavior as the 2DEG density increases. Based on this factor, three analytical regimes are derived, corresponding to the low-, moderate-, and strong-2DEG regions. Experimental measurements from 300 K to 420 K support the proposed model, verify the three-regime evolution of $1/f$ noise, and identify the CNF–CMF transition boundary through the non-monotonic Hooge parameter. This work provides a unified physical interpretation of gate-bias- and temperature-dependent $1/f$ noise in p-GaN gate HEMTs and offers a basis for trap characterization, low-noise bias optimization, and reliability assessment of GaN power devices.

Appendix A: 2DEG electrostatics and charge-control formulation

For the p-GaN gate AlGaN/GaN HEMTs, when a positive gate voltage V_{GS} is applied, the local gate-voltage balance can be expressed as

$$V_{GS} - V_{TH} - V_c = \Delta\varphi_{Sch} + \Delta\varphi_B + \phi_q, \tag{A1}$$

where $\Delta\varphi_{Sch}$ is the voltage variation across the p-GaN Schottky depletion region, $\Delta\varphi_B$ is the voltage variation across the AlGaN barrier, and ϕ_q is the quantum-confinement-related potential term. For the p-GaN cap layer, the initial depletion potential is

$$V_{bi} = \frac{qN_A t_{d0}^2}{2\varepsilon_{GaN}}, \tag{A2}$$

where N_A is the Mg acceptor concentration, t_{d0} is the initial depletion thickness, and ε_{GaN} is the dielectric permittivity of GaN. After the gate bias is applied, the additional depletion thickness satisfies $\Delta t = n_c/N_A$. The Schottky depletion poten-

CPB Online In-Press

tial variation becomes

$$\Delta\varphi_{\mathrm{Sch}} = \frac{qN_{\mathrm{A}}}{2\varepsilon_{\mathrm{GaN}}}\left(\frac{n_{\mathrm{c}}^2}{N_{\mathrm{A}}^2} + \frac{2n_{\mathrm{c}}t_{\mathrm{d0}}}{N_{\mathrm{A}}}\right). \tag{A3}$$

The voltage variation across the AlGaN barrier is $\Delta\varphi_{\mathrm{B}} = q(\sigma - n_{\mathrm{c}})d/\varepsilon_{\mathrm{AlGaN}}$, where σ is the effective polarization charge density, d is the AlGaN barrier thickness, and $\varepsilon_{\mathrm{AlGaN}}$ is the dielectric permittivity of AlGaN. At the AlGaN/GaN heterointerface, the 2DEG is confined in a triangular quantum well. Considering the first two subbands, the 2DEG sheet density is expressed as

$$n_{\mathrm{c}} = DV_{\mathrm{T}}\left[\ln\left(1+\exp\frac{E_{\mathrm{F}}-E_0}{V_{\mathrm{T}}}\right)+\ln\left(1+\exp\frac{E_{\mathrm{F}}-E_1}{V_{\mathrm{T}}}\right)\right], \tag{A4}$$

where $D = m^*/(\pi\hbar^2)$ is the two-dimensional density of states, E_{F} is the Fermi level, and $E_{\mathrm{i}} = \gamma_{\mathrm{i}}(\hbar^2/2m^*)^{1/3}(3\pi q^2 n_{\mathrm{c}}/2\varepsilon_{\mathrm{GaN}})^{2/3}$ with $\gamma_0 \approx 2.338$ and $\gamma_1 \approx 4.008$. Equation (A4) describes the evolution of the 2DEG density as the Fermi level approaches and successively populates the confined subbands.

The drain-to-source current is described using a variable-channel approximation:

$$I_{\mathrm{DS}} = \varepsilon_{\mathrm{eff}}\mu_{\mathrm{n}}\frac{W}{L}\left[(V_{\mathrm{GS}} - V_{\mathrm{TH}})\,\varphi - \frac{1}{2}\varphi^2\right], \tag{A5}$$

where $\varepsilon_{\mathrm{eff}}$ is the effective dielectric constant, W is the device width, and L is the gate (channel) length. The electron mobility μ_{n} is written as

$$\mu_{\mathrm{n}} = \frac{\mu_0}{1 + p_1 V_{\mathrm{GT}} + p_2 V_{\mathrm{GT}}^2}, \tag{A6}$$

where μ_0 is the low-field mobility, and p_1 and p_2 are mobility-degradation coefficients.

Appendix B: Trap occupation and relaxation-time distribution

For a single trap, the occupation fluctuation follows the Fermi–Dirac distribution

$$f_{\mathrm{T}}(E,T) = \frac{1}{1+\exp\left[(E-E_{\mathrm{F}})/kT\right]}, \tag{B1}$$

where E is the trap energy level. The fluctuation strength of trap occupation is proportional to $f_{\mathrm{T}}(E,T)[1-f_{\mathrm{T}}(E,T)]$, which indicates that traps close to the Fermi level contribute most strongly to the flicker-noise process.

The trap emission time constant is expressed as

$$\tau(z) = \tau_0 \exp\left(\frac{E_{\mathrm{a}}}{kT}\right)\exp(2\gamma z), \tag{B2}$$

where τ_0 is the pre-exponential time constant, E_{a} is the trap activation energy, and z is the trap distance from the channel. For a distributed trap ensemble, the fluctuation spectrum is obtained from the superposition of Lorentzian spectra:

$$S_{\delta\mathrm{NT}}(f) = \int \frac{4\tau}{1+\omega^2\tau^2} D_{\mathrm{T}}(E,z)\,\mathrm{d}E\,\mathrm{d}z, \tag{B3}$$

where $\omega = 2\pi f$ is the angular frequency, and $D_{\mathrm{T}}(E,z)$ is the spatial and energetic trap distribution. For a broad distribution of trap time constants, the superposed Lorentzian spectra approach an effective $1/f^{\gamma}$ dependence over a finite frequency window. The value of γ can vary with frequency and temperature because the active relaxation-time window depends on trap energy, position, and occupation.

Over a finite frequency window, the integration of Eq. (B3) over a broad distribution of trap energies and positions can be represented by

$$S_{\delta\mathrm{NT}}(f) = \frac{kT}{\lambda_{\mathrm{t}} f^{\gamma}} N_{\mathrm{T}}(E_{\mathrm{F}},T), \tag{B4}$$

which is the trap-occupation spectrum used in Eq. (3).

Acknowledgements

This work was supported by the National Natural Science Foundation of China (Grant Nos. 62374045, 61404110, and U2469204), the Key-Area Research and Development Program of Guangdong Province (Grant No. 2024B0101060002), the Natural Science Foundation of Guangdong Province (Grant No. 2024A1515010852), the Guangzhou Basic and Applied Basic Research Project (Grant No. 2024A04J001), the State Key Laboratory Special Fund of China Electronic Product Reliability and Environmental Testing Research Institute (Grant No. 24D04), and the Key Research and Development Support Foundation (Grant Nos. 2025-YF11-00007-HZ and 2024-YF08-00041-GX).

References

[1] Meneghini M, Santi C D, Abid I, Buffolo M, Cioni M, Khadar R A, Nela L, Zagni N, Chini A, Medjdoub F, Meneghesso G, Verzellesi G, Zanoni E and Matioli E 2021 *J. Appl. Phys.* **130** 181101
[2] Wang Z G, Chen W J, Zhang J, Zhang B and Li Z J 2012 *Chin. Phys. B* **21** 087305
[3] Xie X T, Zhang C, Zhao Z J, Wei J, Luo X R and Zhang B 2023 *Chin. Phys. B* **32** 098506
[4] Shi Y J, He Z Y, Huang Y, Cai Z Q, Chen Y Q, Cheng L Y, Chen W J, Sun R Z, Liu C, Lu G G and Zhang B 2023 *IEEE Trans. Electron Devices* **70** 2229
[5] Shen J Y, Yang C, Liang J, Li P, Wu H, Huang Z Y and Hu S D 2023 *IEEE Trans. Power Electron.* **38** 6073
[6] Shen J Y, Yang C, Liang J, Guo J W, Li P, Wu H and Hu S D 2024 *IEEE Trans. Electron Devices* **71** 1523
[7] Peng R, Huang S T, Qiu B J, Chen K L, Xiong Q, Zhou J G, Zhu J G, Yang N, Tang L, Duan E C, Zhou C H, Zhang B and Zhou Q 2026 *IEEE Trans. Power Electron.* **41** 12769
[8] Shi Y J, Zhao D S, Shen Z P, Wu L J, He L, Jiang X C, Yang G L, Xiao Q Z, Chen X H, Chen Y and Lu G G 2025 *IEEE Trans. Electron Devices* **72** 4810
[9] Zhou J G, Tang L, Peng R, Qiu B J, Gao H, Huang S T, Zhu J G, Yang N, Chen K L, Zhang B and Zhou Q 2025 *IEEE Trans. Electron Devices* **73** 215
[10] Silvestri M, Uren M J, Killat N, Marcon D and Kuball M 2013 *Appl. Phys. Lett.* **103** 043506

CPB Online In-Press

[11] Asanovski R, Palestri P, Caruso E and Selmi L 2021 *IEEE Trans. Electron Devices* **68** 4826

[12] Vandamme L K J and Hooge F N 2008 *IEEE Trans. Electron Devices* **55** 3070

[13] Sai P, Jorudas J, Dub M, Sakowicz M, Jakštas V, But D B, Prystawko P, Cywinski G, Kašalynas I, Knap W and Rumyantsev S 2019 *Appl. Phys. Lett.* **115** 183501

[14] Wu J J, Ren P P and Ji Z G 2023 *IEEE Trans. Electron Devices* **70** 6078

[15] Crupi F, Magnone P, Strangio S, Iucolano F and Meneghesso G 2016 *IEEE Trans. Electron Devices* **63** 2219

[16] Johari A, Gupta A, Wu T L and Singh R 2025 *IEEE J. Electron Devices Soc.* **13** 870

[17] Samnakay R, Balandin A A and Srinivasan P 2017 *Solid-State Electron.* **135** 37

[18] Chen Q, Chen Y Q, Liu C, He Z Y, Chen Y, Ceng K W, He Y J and Chen W Y 2024 *IEEE J. Electron Devices Soc.* **12** 698

[19] Chen H Y, Lee H Y and Lee C T 2026 *J. Electron. Mater.* **55** 6301

[20] Wong H 2003 *Microelectron. Rel.* **43** 585

[21] Liu T K, Lee H, Luo X Y, Zhang E X, Schrimpf R D, Rajan S and Fleetwood D M 2024 *J. Appl. Phys.* **136** 145702

[22] Takakura K, Putcha V, Simoen E, Alian A R, Peralagu U, Waldron N, Parvais B and Collaert N 2020 *IEEE Trans. Electron Devices* **67** 3062

[23] Nazir M S, Pampori A, Dangi R, Ahsan S A and Chauhan Y S 2023 *IEEE Electron Device Lett.* **44** 1416

[24] Nsele S D, Escotte L, Tartarin J G, Piotrowicz S and Delage S L 2014 *Appl. Phys. Lett.* **105** 192105

[25] Berntgen J, Heime K, Daumann W, Auer U, Tegude F J and Matulionis A 1999 *IEEE Trans. Electron Devices* **46** 194

[26] Dasgupta A, Khandelwal S and Chauhan Y S 2014 *IEEE J. Electron Devices Soc.* **2** 174

[27] Lim J S, Acosta A, Thompson S E, Bosman G, Simoen E and Nishida T 2009 *J. Appl. Phys.* **105** 054504

[28] Kammeugne R K, Theodorou C, Leroux C, Vauche L, Mescot X, Gwoziecki R, Becu S, Charles M, Bano E and Ghibaudo G 2023 *Solid-State Electron.* **200** 108555

[29] Fleetwood D M 2023 *Appl. Phys. Lett.* **122** 173504

[30] Primarius Technologies Co., Ltd. *FS-Pro: All-In-One Semiconductor Parameter Analyzer*, Product Datasheet. [Online]. Available: Primarius Technologies official website

[31] Bonaldo S, Putcha V, Linten D, Pantelides S T, Reed R A, Schrimpf R D, Fleetwood D M, Zhao S E, O'Hara A, Gorchichko M, Zhang E X, Gerardin S, Paccagnella A, Waldron N and Collaert N 2020 *IEEE Trans. Nuclear Science* **67** 210

[32] Wang P, Jiang R, Chen J, Zhang E X, McCurdy M W, Schrimpf R D and Fleetwood D M 2017 *IEEE Trans. Nuclear Science* **64** 181

CPB Online In-Press